




## Article

# The Role of Er<sup>3+</sup> Content in the Luminescence Properties of Y<sub>3</sub>Al<sub>5</sub>O<sub>12</sub> Single Crystals: Incorporation into the Lattice and Defect State Creation

Maksym Buryi <sup>1,2,\*</sup>, Amayès Médhi Gaston-Bellegarde <sup>1,2</sup>, Jan Pejchal <sup>1</sup> , Fedor Levchenko <sup>1,3</sup>, Zdeněk Remeš <sup>1</sup> , Katarína Ridzoňová <sup>1,4</sup>, Vladimír Babin <sup>1</sup> and Sergii Chertopalov <sup>1</sup> 

- <sup>1</sup> FZU—Institute of Physics of the Czech Academy of Sciences, Na Slovance 1999/2, 182 00 Prague, Czech Republic; gastonbellegarde@fzu.cz (A.M.G.-B.)
- <sup>2</sup> Faculty of Nuclear Sciences and Physical Engineering, Brehova 7, 115 19 Prague, Czech Republic
- <sup>3</sup> Department of Inorganic Chemistry, University of Chemistry and Technology, Technická 5, 166 28 Prague, Czech Republic
- <sup>4</sup> Faculty of Mathematics and Physics, Institute of Physics, Charles University, Ke Karlovu 5, 121 16 Prague, Czech Republic
- \* Correspondence: buryi@fzu.cz

**Abstract:** Erbium-doped Y<sub>3</sub>Al<sub>5</sub>O<sub>12</sub> (YAG) single crystals grown using the micro-pulling-down technique were investigated. Three Er concentrations were chosen: 0.1, 0.3 and 1 at%. Er<sup>3+</sup> electron paramagnetic resonance (EPR) spectra were measured in the ground and first excited states. The corresponding *g* tensors and <sup>167</sup>Er hyperfine interaction were changing upon Er content indicating moderation of the Er-O bond length and/or Er local surrounding. Photoluminescence (PL) and radioluminescence (RL) spectra were complex, consisting of strongly overlapped typical Er<sup>3+</sup> transitions. In addition, there were other broad PL band (3.1 eV) and RL band (3.95 eV) attributed to the F<sup>+</sup> center and yttrium substituting for aluminum (Y<sub>Al</sub>), respectively. The X-ray excited decay kinetics exhibited a decrease of the decay time of the Y<sub>Al</sub> from hundreds of nanoseconds to nanoseconds upon Er doping level. This is discussed and explained considering EPR data.

**Keywords:** yttrium aluminum garnet; erbium doping; EPR; luminescence; kinetics



**Citation:** Buryi, M.; Gaston-Bellegarde, A.M.; Pejchal, J.; Levchenko, F.; Remeš, Z.; Ridzoňová, K.; Babin, V.; Chertopalov, S. The Role of Er<sup>3+</sup> Content in the Luminescence Properties of Y<sub>3</sub>Al<sub>5</sub>O<sub>12</sub> Single Crystals: Incorporation into the Lattice and Defect State Creation. *Crystals* **2023**, *13*, 562. <https://doi.org/10.3390/cryst13040562>

Academic Editors: Maria Milanova and Martin Tsvetkov

Received: 28 February 2023

Revised: 16 March 2023

Accepted: 18 March 2023

Published: 25 March 2023



**Copyright:** © 2023 by the authors. Licensee MDPI, Basel, Switzerland. This article is an open access article distributed under the terms and conditions of the Creative Commons Attribution (CC BY) license (<https://creativecommons.org/licenses/by/4.0/>).

## 1. Introduction

Yttrium aluminium garnet (Y<sub>3</sub>Al<sub>5</sub>O<sub>12</sub>; YAG) is a synthetic crystalline material, known for its excellent optical properties (especially when doped with a luminescent ion) and mechanical, chemical and temperature stability [1–3]. In practice, YAG is doped with different rare earth ions, such as Nd, Er, Ce and Tm, to obtain new chemical/physical properties, thus, making YAG feasible for lasers, light emitters and scintillators [4]. The main application of YAG:X (X = Nd, Er or Tm) is in medicine for laser treatment (dermatology [5], ophthalmology [6], blood sugar monitoring [7], etc.).

Er ions with deep infrared luminescence (1.55 μm) and, specifically, absorption bands at 600 and 800 nm are especially suitable for lasing applications as a YAG:Er laser emits at 2940 nm [5,8–11]. This wavelength is strongly absorbed by water/body fluids [12] making it suitable for a large branch of medical applications, such as skin disease or as monitoring medical procedures (making them less invasive). In addition, YAG:Er laser wavelength is also absorbed by hydroxyapatite [12] making it able to cut bones or soft tissues [13]. These properties are exceedingly useful for oral surgery and otolaryngology [12,14–16]. Moreover, YAG:Er is also used as a dental laser [13], because it has a sedative effect on the nerves leading to painless dental surgeries.

Many studies in the last decade were dedicated to optical characterization (absorption and luminescence, including upconversion and decay kinetics) of YAG:Er in different material forms (single crystals (stoichiometric and non-stoichiometric), thin films and

micro- and nanoparticles), see, e.g., [1,3,4,17–19]. To the best of our knowledge, there is only one relatively recent work focused on EPR characterization of YAG:Er [20]. In particular, it was shown that, in YAG:Er,  $\text{Er}^{3+}$  can be found in its ground state or in its first excited state.

The  $g$  tensor values were determined as follows  $g_1 = 7.75$ ,  $g_2 = 7.35$  and  $g_3 = 3.71$  for the  $\text{Er}^{3+}$  in the ground state and  $g_1 = 2.036$ ,  $g_2 = 1.995$  and  $g_3 = 14.6$  for the  $\text{Er}^{3+}$  in the first excited state. At the same time, the hyperfine tensors of  $\text{Er}^{3+}$  ions in both the ground and first excited states were not determined. Moreover, there is not a single work reporting on luminescence properties correlated with the EPR characterization, especially considering the determination of Er distribution and defect states creation in YAG:Er as a function of Er content.

The influence of Er local surrounding on luminescence properties is, thus, unknown. Therefore, these are the aims of the present work. In addition, it is commonly known that antisite defects degrade scintillating performance. In contrast, in the present study, we demonstrate that the luminescence band generated by yttrium-aluminum antisite can be accelerated to the order of nanoseconds by increased erbium content.

## 2. Experimental

### 2.1. Samples Preparation

The YAG:Er crystals were grown by the micro-pulling-down method [21,22] with radiofrequency inductive heating. The growth was performed using an Ir crucible with a circular die of 3 mm in diameter and a nozzle diameter of 0.5 mm under a  $\text{N}_2$  (4N) atmosphere using the  $\langle 111 \rangle$  oriented YAG single crystal as a seed. The crucible was placed on an Ir after-heater with windows and an alumina pedestal. The hot zone around the crucible consisted of three layers of alumina shielding for thermal insulation. The gas flow was always kept at 0.5 L/min.

The crucible with the starting material composed of stoichiometric mixture of  $\text{Y}_2\text{O}_3$ ,  $\text{Al}_2\text{O}_3$  and  $\text{Er}_2\text{O}_3$  powders (4N) was heated up to the YAG melting temperature, which was around 1940 °C. Then, the YAG single-crystal seed was brought into contact with the melt coming through the nozzle due to the capillary action. The pulling speed was 0.1 mm/min. In all of the growth attempts, it was possible to pull out all the melt. The crystal rods had a diameter of 3 mm and were around 30 mm in length. Afterwards, the samples were ground to powders.

### 2.2. Experimental Techniques

X-ray diffraction (XRD) patterns (Rigaku Innovative Technologies Europe s.r.o., Dolní Břežany, Czech Republic) were obtained within the 20–80° range of angles (a step of 0.02° and a scanning rate of 2°/min were used) on a Rigaku Miniflex 600 diffractometer coupled with the Cu X-ray tube operating at a wavelength  $K_{\alpha 1,2}$  of 0.15418 nm, a voltage of 40 kV and a current of 15 mA. The ICDD PDF-2 database (version 2013) was used for comparison.

The diffraction patterns were processed by Rietveld Refinement program Topas 3 to perform fast sequential and parametric whole powder profile refinement of in situ time-resolved powder diffraction data [23]. The phase composition was given by structure fit, where intensities of peaks were calculated based on the atomic position in the unit cell (the atomic positions were not refined). Scherrer law was used.

Photoluminescence characteristics were measured on a homemade spectrometer composed of: (a) a pulsed UV light-emitting diode (LED) operating at 340 nm wavelength and 1 mW power; (b) a narrow UV band-pass optical filter; (c) a spectrally calibrated double-grating monochromator SPEX 1672; (d) long-pass filters; (e) a Peltier cooled photomultiplier sensitive in the 350–750 nm spectral range with 2 nm spectral resolution; (f) a picoammeter as a current amplifier ( $10^5$  V/A); and (g) a lock-in amplifier referenced to the LED frequency (307 Hz) [24,25].

The IR PL spectra were measured at room temperature with a 1  $\text{cm}^{-1}$  spectral resolution using a Nicolet™ iS50 FTIR Spectrometer (Thermo Fisher Scientific, Waltham, MA,

USA) equipped with 980 nm laser diode, 50 mW laser power, CaF<sub>2</sub> beamsplitter, InGaAs photodiode as a detector and a scan rate of 0.3165 cm/s.

The radioluminescence was measured using the Horiba Jobin-Yvon 5000 M spectrometer (Horiba Scientific, Glasgow, UK) with Oxford liquid nitrogen cryostat and TBX-04 (IBH) photomultiplier operating in the 200–800 nm spectral range. The spectral resolution of the monochromator was 8 nm. All the spectra were corrected for experimental distortions caused by the setup. The samples were irradiated by a Seifert X-ray tube operated at 40 kV with a tungsten target. The RL spectra were measured at 300 and 77 K. All PL and RL spectra were converted from wavelength to energy scale taking into account the Jacobian correction [26].

Ultrafast decays under pulsing X-ray excitation (Hamamatsu Photonics, Hamamatsu City, Japan) were measured using picosecond (ps) X-ray tube N5084 (Hamamatsu, 40 kV). The X-ray tube is driven by the ps light pulser equipped with a laser with the repetition rate up to 1 MHz. The signal was detected by hybrid picosecond photon detector and Fluorohub unit (Horiba Scientific, Glasgow, UK). The instrumental response time was about 75 ps. The spectrally unresolved luminescence decay curves were detected from the same side where they were excited by X-rays. The decay curves were recorded by means of the time-correlated single photon counting method. The true decay times were obtained using the convolution of the instrumental response with a multiexponential function using the Spectra Solve software package (Ames Photonics, Hurst, TX, USA).

Electron paramagnetic resonance (EPR) (Bruker, Billerica, MA, USA) measurements were performed on a commercial Bruker EMXplus spectrometer (X-band with a 9.4 GHz frequency) with a sensitivity of around 10<sup>12</sup> spins/mT. The temperature range was 10–296 K (Oxford Instruments ESR900 cryostat was used). The “Easyspin 5.2.35” program toolbox [27] was used for all spectra simulations.

### 3. Results and Discussion

#### 3.1. Phase Purity by XRD

To determine whether the grown samples were phase purity Y<sub>3</sub>Al<sub>5</sub>O<sub>12</sub> (YAG), powder XRD was applied. The corresponding patterns are shown in Figure 1. It can be seen that the reflections are the same in all three samples, and they correspond to the pure cubic (Ia $\bar{3}$ d) YAG phase (no other phases were detected). From this, it also follows that, in general, the incorporation of Er does not affect the crystal lattice parameter. The crystallite size was determined to be in the range 0.002–5  $\mu$ m in all the YAG:Er samples.

#### 3.2. Paramagnetic Defect States and Er Incorporation by EPR

EPR spectra measured at room temperature are shown in Figure 2A. They were composed of one signal found at the  $g$  factor  $g \sim 2$  relevant for the present study.

This signal is different in different samples—S1 in YAG:Er (0.1%), S2 in YAG:Er (0.3%) and S3 in YAG:Er (1%) as shown in Figure 2A. Moreover, the signals intensity is lower upon Er content. To obtain better insight into the structure of these signals, they were fitted. The following spin-Hamiltonian was used for this purpose:

$$\hat{H} = \beta \hat{S} \hat{g} H, \quad (1)$$

where  $\beta$ ,  $\hat{S}$ ,  $\hat{g}$  and  $H$  are the Bohr magneton; electron spin operator ( $S = \frac{1}{2}$  since no other complementary resonances to those in Figure 2A were observed);  $g$  tensor with the principal values  $g_1$ ,  $g_2$  and  $g_3$  (variable parameters); and magnetic field, respectively. The results of fit are given in Table 1.

As one can see, the  $g$  tensor values are different for the S1–S3 signals. In the case of the S1, the  $g_1 = g_2 = g_{\perp}$ , and it is larger than 2.0023. The free electron value while the  $g_3 = g_{\parallel}$  is lower than 2.0023. This is typical for the O<sub>2</sub><sup>−</sup> oxygen complexes [28,29]. The  $|g_{\parallel} - g_{\perp}| = 0.023$ . In contrast, in the case of the S2, despite the equality of the  $g_{1,2} = g_{\perp}$ , this value is only slightly lower than 2.0023 while the  $g_3$  is larger than 2.0023. This can be, in principle, an O<sup>−</sup> defect, the oxygen anion captured a hole in the presence

of some local perturbation, such as the cation vacancy lowering bonding as reported for CaO (for more details, see, e.g., [30]).

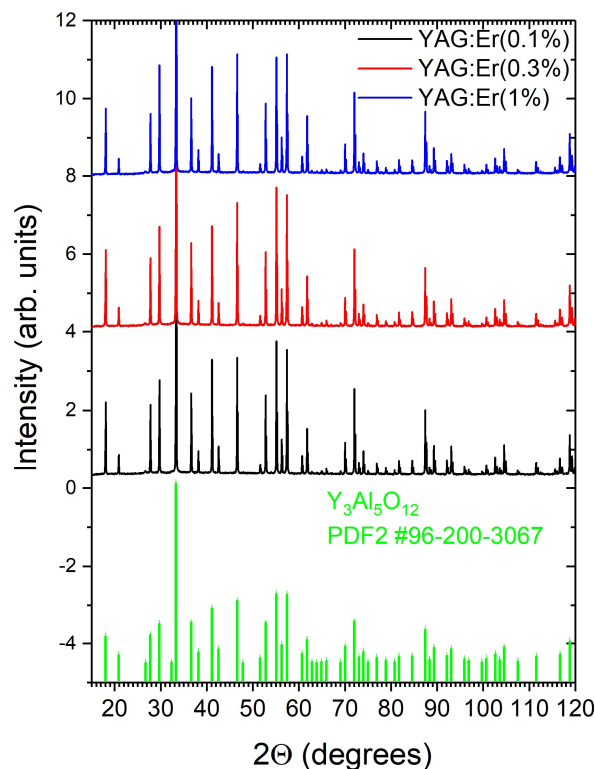


**Figure 1.** XRD patterns of the YAG:Er (0.1, 0.3 and 1%) samples (indicated in the legend). The PDF2 record #96-200-3067 is also shown.

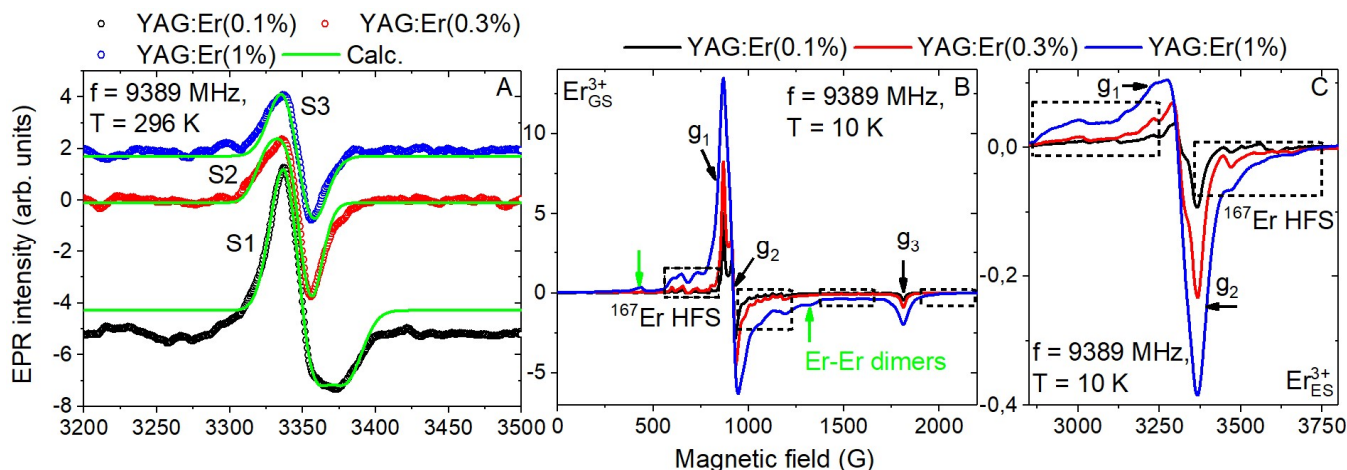


**Figure 2.** (A) Experimental EPR S1-3 signals measured in the YAG:Er (0.1, 0.3 and 1%) samples at 296 K shown along with the calculated ones. (B) Experimental EPR spectra of  $\text{Er}^{3+}$  in the ground state ( $\text{Er}_{\text{GS}}^{3+}$ ) measured in the YAG:Er (0.1, 0.3 and 1%) samples at 10 K.  $g_{1-3}$ , and arrows indicate the spectral position of the  $g$  tensor values contributions. Dashed oblongs stress hyperfine structure (HFS) due to  $^{167}\text{Er}$  nucleus. Green vertical “up” and “down” arrows point out the doublets due to the Er–Er dimer creation. (C) Experimental EPR spectra of  $\text{Er}^{3+}$  in the first excited state ( $\text{Er}_{\text{ES}}^{3+}$ ) measured in the YAG:Er (0.1, 0.3 and 1%) samples at 10 K.  $g_{1,2}$  and arrows indicate the spectral position of the  $g$  tensor values contributions. Dashed oblongs stress HFS due to the  $^{167}\text{Er}$  nucleus.

**Table 1.** Spin-Hamiltonian parameters from Equation (1). The error of  $g_i$  ( $i = 1-3$ ) determination is  $\pm 0.0005$ .

Sample	Signal	$g_1$	$g_2$	$g_3$
YAG:Er (0.1%)	S1	2.0070	2.0070	1.9840
YAG:Er (0.3%)	S2	2.0014	2.0014	2.0170
YAG:Er (1%)	S3	2.0045	2.0045	2.0045

The  $|g_{||} - g_{\perp}| = 0.0156$ . The S3 signal is isotropic and its  $g_{iso} = g_1 = g_2 = g_3 = g_{||} = g_{\perp}$  is slightly larger than 2.0023. Again, it is expected to be produced by the  $O^-$  defect as well. Formally, in this case, the  $|g_{||} - g_{\perp}| = 0$ . All of these indicates that Er improves the defect structure of the YAG lattice. The yttrium vacancies likely become filled in with Er, and as a result, the cation related  $O^-$  defects cannot appear. Note that  $Er_3Al_5O_{12}$  (EAG) garnet exists [31,32], and therefore erbium incorporation into the garnet host is natural.  $Er^{3+}$  is paramagnetic with a short relaxation constant.

Therefore, it is very well observed at temperatures below 15 K [33,34]. The  $Er^{3+}$  spectrum with perfect spectral resolution was presently measured in all the YAG:Er samples. Moreover, its integral intensity exhibited linear dependence on the Er doping level. This is shown in Figure 2B. It is classical, especially considering the clearly visible hyperfine structure from  $^{167}Er$  nucleus with the nuclear spin  $I = 7/2$  and natural abundance of about 23% as stressed in Figure 2B. The  $Er^{3+}$  has three unpaired electrons in the outer  $4f^{11}$  shell.

However, the splitting between Kramers doublets in this case is too high—much larger than the microwave quantum energy in the spectrometer used. Therefore, only the effective spin  $\tilde{S} = \frac{1}{2}2$  of the lowest one can be observed experimentally. Due to this reason, the  $Er^{3+}$  powder spectra of the three YAG:Er samples in Figure 2B have all features of the typical three-component rhombic powder spectrum [35]. The spectrum in Figure 2B is typical for  $Er^{3+}$  in the ground ion state, i.e.,  $^4I_{15/2}$ ,  $Er_{GS}^{3+}$ .

Spectral positions of these components correspond to the principal values of a  $g$  tensor. The  $Er_{GS}^{3+}$  signal becomes broader upon Er content due to the dipolar mechanism [35]. Moreover, a doublet of lines becomes clearly visible in the YAG:Er (1%) beside the first two partly overlapping characteristic components ( $g_{1,2}$  in Figure 2B), which can be ascribed to the  $Er^{3+}-Er^{3+}$  dimer.

Another signal whose intensity had the same temperature dependence as well as the dependence on Er doping level as the  $Er_{GS}^{3+}$  one was measured at the  $g$  factor  $\sim 2$  (Figure 2C). Therefore, it is expected to originate from Er as well. It is much weaker (about 30 times) than the  $Er_{GS}^{3+}$  one (Figure 2B,C).

Since the spectral positions of both the  $Er_{GS}^{3+}$  and the new Er signal are very different (Figure 2B,C) and considering the fact that the typical spectral position of Er EPR signal is that of the  $Er_{GS}^{3+}$  (see also [20,34]), the new erbium related signal in Figure 2C was attributed to the  $Er^{3+}$  found in the first excited state,  $^4I_{13/2}$ . It is stressed as the  $Er_{ES}^{3+}$  in Figure 2C.

To obtain more information about Er incorporation into the YAG host and to determine the spectral parameters, first, the  $Er_{GS}^{3+}$  signal (Figure 2B) was fitted in all the YAG:Er samples using the following spin-Hamiltonian (the natural abundance of  $^{167}Er$  was considered):

$$\hat{H} = \beta \hat{S} \hat{g} H + \hat{S} \hat{A} \hat{I} + \hat{I} \hat{Q} \hat{I}, \quad (2)$$

where  $\hat{A}$ ,  $\hat{Q}$  and  $\hat{I}$  are hyperfine and quadrupolar tensors with the principal values  $A_1$ ,  $A_2$  and  $A_3$  and  $Q_1$ ,  $Q_2$  and  $Q_3$  (variable parameters) and nuclear spin operator (for  $^{167}Er$   $I = 7/2$ ), respectively. The experimental signals as well as fitting curves are shown in Figure 3A,B on an example of a YAG:Er (0.1%) sample where the line  $Er^{3+}$  resonance line broadening is the smallest, and the resolution is the best. The results of the fit are given in Table 2.

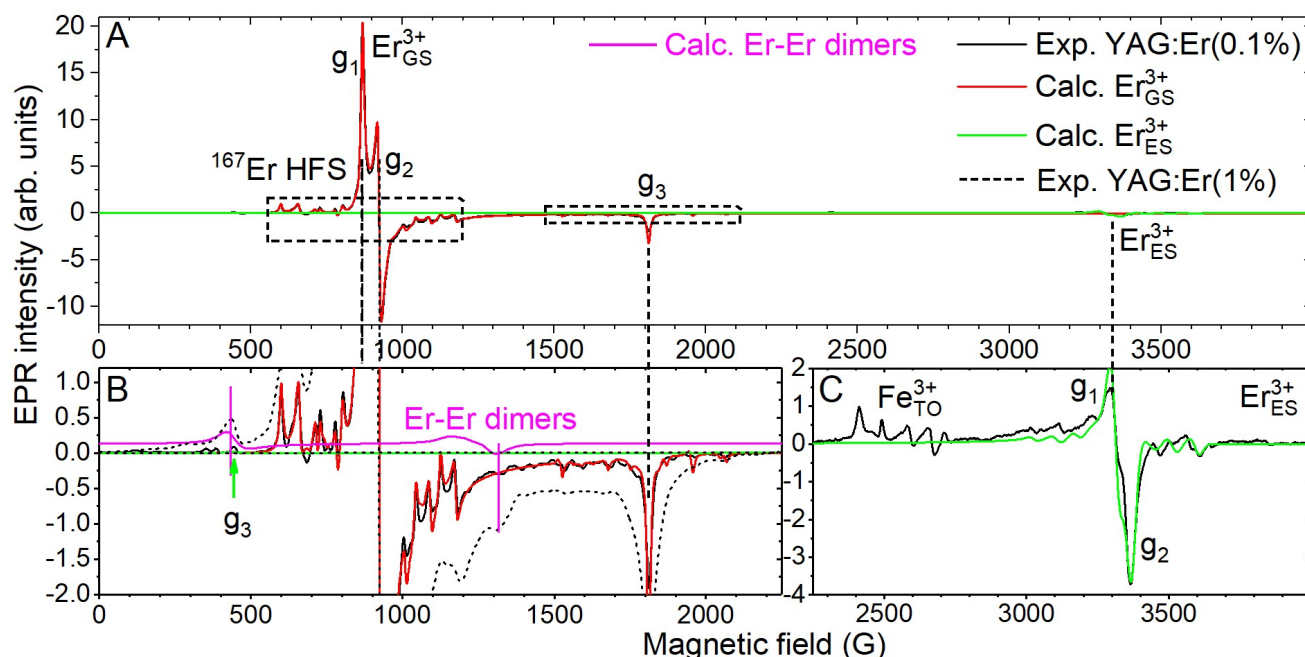


**Figure 3.** (A) Experimental EPR  $\text{Er}_{\text{GS}}^{3+}$  and  $\text{Er}_{\text{ES}}^{3+}$  signals measured in the YAG:Er (0.1%) samples at 10 K shown along with the calculated ones (see the legend). (B,C) Closeups of the panel A. Additionally, the closeup of the experimental YAG:Er (1%) spectrum as well as calculated Er–Er dimers are also indicated.  $g_{1-3}$  and arrows indicate the spectral position of the  $g$  tensor values contributions for both  $\text{Er}_{\text{GS}}^{3+}$  and  $\text{Er}_{\text{ES}}^{3+}$ . Dashed oblongs stress hyperfine structure (HFS) due to  $^{167}\text{Er}$  nucleus.

**Table 2.** Spin-Hamiltonian parameters from Equations (2) and (3). The error of  $g_i$  ( $i = 1-3$ ) determination is  $\pm 0.0005$ . The error of  $A_i$  ( $i = 1-3$ ) determination is  $\pm 10$ . The error of  $Q_i$  ( $i = 1-3$ ) determination is  $\pm 1$ . The error of  $K_i$  ( $i = 1-3$ ) determination is  $\pm 1$ .  $K_i$  is related only to the Er–Er dimer.

Sample	Signal	$g_1$	$g_2$	$g_3$	$A_1$	$A_2$	$A_3$	$K_1/Q_1$	$K_2/Q_2$	$K_3/Q_3$
YAG:Er (0.1%)		7.718	7.258	3.702	800	740	390	10	2	50
YAG:Er (0.3%)	$\text{Er}_{\text{GS}}^{3+}$	7.718	7.268	3.700	790	740	400	10	−20	50
YAG:Er (1%)		7.745	7.288	3.701	790	740	400	10	−20	50
YAG:Er (0.1%)		2.025	1.991	15.3	230	190	180	-	-	-
YAG:Er (0.3%)	$\text{Er}_{\text{ES}}^{3+}$	2.025	1.991	15.3	240	230	180	-	-	-
YAG:Er (1%)		2.025	1.991	15.3	240	230	180	-	-	-
YAG:Er (1%)	Er–Er	7.745	7.288	3.401	-	-	-	19,300	19,300	5000

The fit is good (Figure 3A,B). The  $g$  tensor parameters presently determined (Equation (2)) are close to those reported previously for  $\text{Er}^{3+}$  in Czochralski-grown YAG:Er (0.1%) ( $g_1 = 7.75$ ,  $g_2 = 7.35$  and  $g_3 = 3.71$ ) [20] but still different (see Table 2). The  $g_3$  is oriented along the  $\langle 100 \rangle$  axis whereas the  $g_{1,2}$  are oriented along the  $\langle 110 \rangle$  axes [20]. There is a clearly observed trend—the  $g_{1,2}$  values are increasing with the Er content (Table 2). This tendency has never been reported before.

Since EAG exists [31] and the lattice parameters of EAG (11.9928 Å) and YAG (12.0062 Å) [32,36] are different (0.0134 Å), the Er-O bond length will also be different. Therefore, the Er-O bond length becomes moderated in YAG upon increased Er content. The local crystal field is changing, and the  $g$  factors are changing as well. However, the  $g_3$  remains almost unchanged. This indicates preferable erbium substitution in the YAG lattice in the way that the tension appears along the  $\langle 110 \rangle$  axes. Remarkably, the determined hyperfine constants  $A_{1,3}$  as well as quadrupolar  $Q_2$  are changing also (Table 2). Similar explanation is appropriate.

The Er–Er dimer doublet of lines is most clearly visible in the EPR spectra of YAG:Er (1%) and almost totally absent in the EPR spectra of the rest of samples. To describe it, the exchange and dipolar interactions were considered as one tensor  $\hat{K}$  (with the components  $K_{1-3}$ ) in the following spin-Hamiltonian:

$$\hat{H} = \beta \hat{S}_1 \hat{g}_1 H + \beta \hat{S}_2 \hat{g}_2 H + \hat{S}_1 \hat{K} \hat{S}_2, \quad (3)$$

where  $\hat{S}_{1,2}$   $\hat{g}_{1,2}$  are electron spin operators ( $S_1 = S_2 = \frac{1}{2}2$ ) and the  $\mathbf{g}$  tensors of the two  $\text{Er}^{3+}$  ions creating the Er–Er dimer, respectively. The calculated spectrum as well as experimental one of the YAG:Er (1%) are both shown in Figure 3B. The agreement between them is good. The  $\hat{g}_1 = \hat{g}_2$  was considered. The fit parameters are listed in Table 2. As one can see, the  $g_3$  in this case is smaller than in the case of a single ion. From this, it follows that, most likely, in the dimer, both Er ions are situated at adjacent yttrium sites to create a larger influence on the lattice there. Note that the resonance lines of the dimer are broad, and therefore the (super) hyperfine interaction with  $^{167}\text{Er}$  could not be taken into account.

The  $\text{Er}_{\text{ES}}^{3+}$  signal (Figure 2C) was fitted in all the YAG:Er samples using the spin-Hamiltonian in Equation (2) without the third term since the hyperfine structure (the resonance lines originating from the interaction of the electron spin and  $^{167}\text{Er}$  nucleus) is not clearly visible. The experimental signals as well as fitting curves are shown in Figure 3A,C again on an example YAG:Er (0.1%) sample. The fit is satisfactory—at least the order of magnitude can be guessed.

The results of the fit are given in Table 2 as well. The  $\mathbf{g}$  tensor parameters presently determined (Equation (2)) are close to those reported for  $\text{Er}^{3+}$  in the first excited state in Czochralski-grown YAG:Er (0.1%) previously ( $g_1 = 2.036$ ,  $g_2 = 1.995$  and  $g_3 = 14.6$ ) [20] but still different (see Table 2). The strongest difference was observed for the  $g_3$  value. In contrast to the  $\text{Er}_{\text{GS}}^{3+}$ , the  $\mathbf{g}$  tensor values remained unchanged in the case of the  $\text{Er}_{\text{ES}}^{3+}$  upon Er content.

However, the determined hyperfine constants  $A_{1,2}$  changed with the erbium concentration (Table 2). This leads to the assumption that the first excited state of  $\text{Er}^{3+}$  is found above the ligand levels creating molecular orbitals with the ground state. Therefore, the Er-O bond length plays a minor role in this case. However, hyperfine interaction occurs with the same nucleus as in the case of  $\text{Er}_{\text{GS}}^{3+}$ . Therefore, the same explanations as given above for the  $\text{Er}_{\text{GS}}^{3+}$  are suitable here as well.

The rest of the signals in Figure 3C ( $\text{Fe}_{\text{TO}}^{3+}$ ) originate from  $\text{Fe}^{3+}$  in tetrahedral and octahedral Al sites. This is unintentional impurity, as studied in many other works (see, e.g., [37]), and therefore it will not further be considered.

### 3.3. Luminescence Properties

Photoluminescence spectra measured in the UV-visible spectral range in all YAG:Er samples under the same conditions are shown in Figure 4A. There are two bands in the PL spectrum of YAG:Er (0.1%). The first one is peaking at about 2.24 eV, and the second, very broad one, has the maximum at about 3.1 eV. The first band was about 1.5-times increased in the PL spectrum of the YAG:Er (0.3%). The presence of the second band at 3.1 eV could not be confirmed any longer as the other strong multicomponent and broad band with the center of gravity found at about 2.88 eV appeared there.

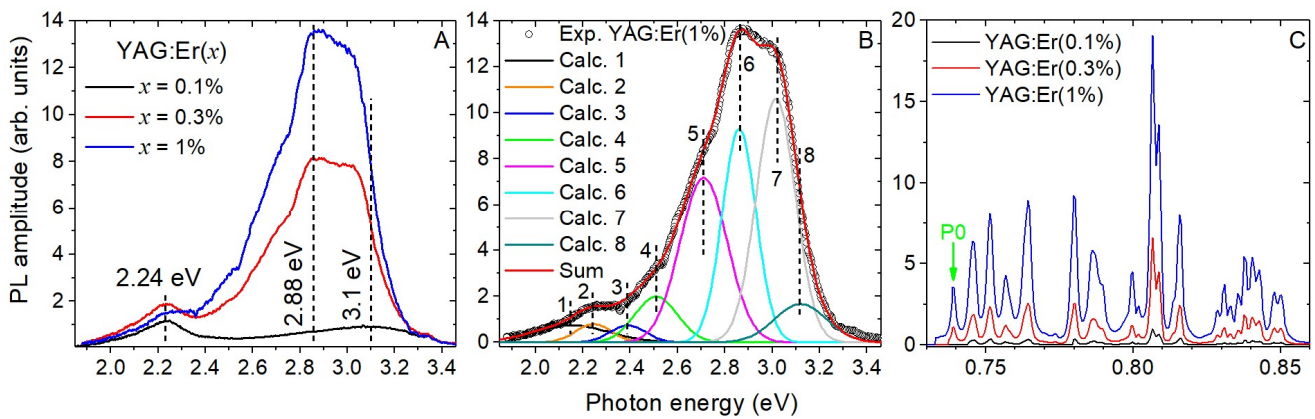


**Figure 4.** (A) PL spectra measured at 296 K under the 340 nm (3.65 eV) LED excitation in the YAG:Er (0.1%, 0.3% and 1%) samples. (B) Experimental PL spectrum of YAG:Er (1%) deconvoluted into Gaussian components (calculated peaks 1–8 as listed in the legend). (C) IR PL spectrum measured under 980 nm (1.27 eV) LED excitation in the YAG:Er (0.1%, 0.3% and 1%) samples. The pronounced structure is due to the Stark transitions [38]. Peak P0 is missing in the IR PL in YAG:Er (1%).

In general, one may expect it to be composed of at least six strongly overlapped contributions. The 2.24 eV band remained about the same in the PL spectrum of the YAG:Er (1%) whereas the 2.88 eV band increased, and its multicomponent origin became even more prominently visible. Since clear correlation between the 2.88 eV band intensity and Er content in the samples was reached, the mentioned six components may originate from broadened  $\text{Er}^{3+}$  4f–4f transitions.

To obtain better insight into the structure of the PL spectra of the YAG:Er (0.1%, 0.3% and 1%) samples, they were deconvoluted into Gaussian components using the following expression:

$$I = \left( I_{0i} / \left( W_i \sqrt{\pi/2} \right) \right) \exp \left( -2 \left( (E - E_i) / W_i \right)^2 \right), \quad (4)$$

where  $E_i$ ,  $W_i$ ,  $I_{0i}$  ( $i = 1-9$ ) are the peak energy maximum, full width at half maximum (FWHM) and amplitude. The fit is shown in Figure 4B on an example of the YAG:Er (1%) sample. The fit parameters are listed in Table 3 for all three YAG:Er samples.

The amplitude ( $I_{0i}$ ) of peaks 3–8 was lowered several times with the decreased Er content (Table 3). Interestingly, the amplitudes of the peaks 1 and 2 remained almost unchanged in the YAG:Er (0.3 and 1%) samples, whereas they dropped about twice in the YAG:Er (0.1%). Based on these considerations and the energy scheme for the  $\text{Er}^{3+}$  ion [38–41], the peaks 3–8 were ascribed to the following  $\text{Er}^{3+}$  4f–4f transitions:  ${}^2\text{H}_{11/2} \rightarrow {}^4\text{I}_{15/2}$  (2.39 eV, peak 3),  ${}^2\text{P}_{3/2} \rightarrow {}^4\text{I}_{11/2}$ ,  ${}^4\text{F}_{7/2} \rightarrow {}^4\text{I}_{15/2}$  (2.51 eV, peak 4),  ${}^4\text{F}_{5/2} \rightarrow {}^4\text{I}_{15/2}$  (2.71 eV, peak 5),  ${}^4\text{F}_{3/2} \rightarrow {}^4\text{I}_{15/2}$  (2.86 eV, peak 6),  ${}^2\text{H}_{9/2} \rightarrow {}^4\text{I}_{15/2}$  (3.02 eV, peak 7) and  ${}^2\text{P}_{3/2} \rightarrow {}^4\text{I}_{13/2}$  (3.12 eV, peak 8). Peak 2 (2.24 eV), most likely originates from the  ${}^4\text{S}_{3/2} \rightarrow {}^4\text{I}_{15/2}$  transition.

The peaks are expected to be composed of a number of Stark transitions. The interplay between the intensity of these transitions results in the slight shift of the peaks 3–8. The peaks are broad, likely, due to the distribution of crystal field parameters where each Er ions is placed at. This is confirmed by the change in the  $g$  and hyperfine tensor principal values in the consequence YAG:Er (0.1%, 0.3% and 1%) as discussed in the subsection above (Table 2). The second reason for the broadening of the Stark transitions in the PL is the interaction between Er ions—coupling, i.e., exchange interaction. This is confirmed by the dipolar broadening of the EPR resonance lines in the section above and the Er–Er dimer creation (see Figures 2 and 3). The exchange interaction leads to advanced charge and energy transfer among erbium ions.



**Table 3.** Fit parameters from Equation (4). The error of  $E_i$  and  $W_i$  ( $i = 1-9$ ) determination is  $\pm 0.03$  eV. The error of the  $I_{0i}$  ( $i = 1-9$ ) determination is  $\pm 3$  arb. units.

Sample	Peak	$E_i$ , eV	$W_i$ , eV	$I_{0i}$ , arb. Units
YAG:Er (0.1%)	1	2.15	0.32	194
	2	2.24	0.15	133
	3	2.39	0.15	30
	4	2.51	0.18	64
	5	2.71	0.20	118
	6	2.86	0.14	77
	7	3.02	0.17	102
	8	3.12	0.22	123
	9	3.25	0.25	150
YAG:Er (0.3%)	1	2.15	0.32	350
	2	2.24	0.15	200
	3	2.39	0.15	60
	4	2.51	0.18	325
	5	2.71	0.20	1104
	6	2.86	0.14	994
	7	3.02	0.17	1276
	8	3.12	0.22	460
	9	-	-	-
YAG:Er (1%)	1	2.15	0.32	300
	2	2.24	0.15	150
	3	2.39	0.15	140
	4	2.51	0.18	530
	5	2.71	0.20	1800
	6	2.86	0.14	1620
	7	3.02	0.17	2080
	8	3.12	0.22	750
	9	-	-	-

Peak 1 is very broad (Figure 4B, Table 3). Its origin is unknown. It is expected to originate from some unintentional impurity. Moreover, there is peak 9 with a maximum at 3.25 eV existing only in the YAG:Er (0.1%). It is too far from the 3.1 eV where the  $F^+$  center (an electron trapped at an oxygen vacancy) emission was reported to appear in YAG [42]. According to [43] it is host-related. However, the exact origin is unknown. It was not observed in the YAG:Er (0.3 and 1%), likely, due to the Er improved reabsorption channel.

A high-resolution infrared PL spectrum of  $Er^{3+} \ ^4I_{13/2} \rightarrow \ ^4I_{15/2}$  transition with perfectly discernible Stark transition is shown in Figure 4C. Logically, the intensity of the transition increases upon erbium content. There are 20 peaks, and the intensity ratio is the following for the YAG:Er (0.1%): 10:11:8:14:6:13:2:19:18:10:9:1:3:2:3:5:5:6:4:4. There are 21 peaks, and the intensity ratio is the following for the YAG:Er (0.3%): 6:6:5:8:5:6:1:15:10:6:4:1:1:1:1:3:3:3:2:2. There are 21 peaks, and the intensity ratio is the following for the YAG:Er (1%): 6:6:5:9:6:7:1:17:10:6:5:1:2:1:2:3:3:4:2:2. The peak P0 is missing in the IR PL spectrum of YAG:Er (0.1%) as indicated in Figure 4C.

Moreover, the peak intensity ratios are strongly different for the YAG:Er (0.1%) as compared to the YAG:Er (0.3 and 1%). It is about the same in the YAG:Er (0.3 and 1%). This again confirms appearance of changes to the local surrounding of Er ions when its content is increasing in the YAG host.

Radioluminescence spectra measured in the UV-visible spectral range in all YAG:Er samples are shown in Figure 5A. There are seven narrow peaks and one broad band at 3.95 eV.

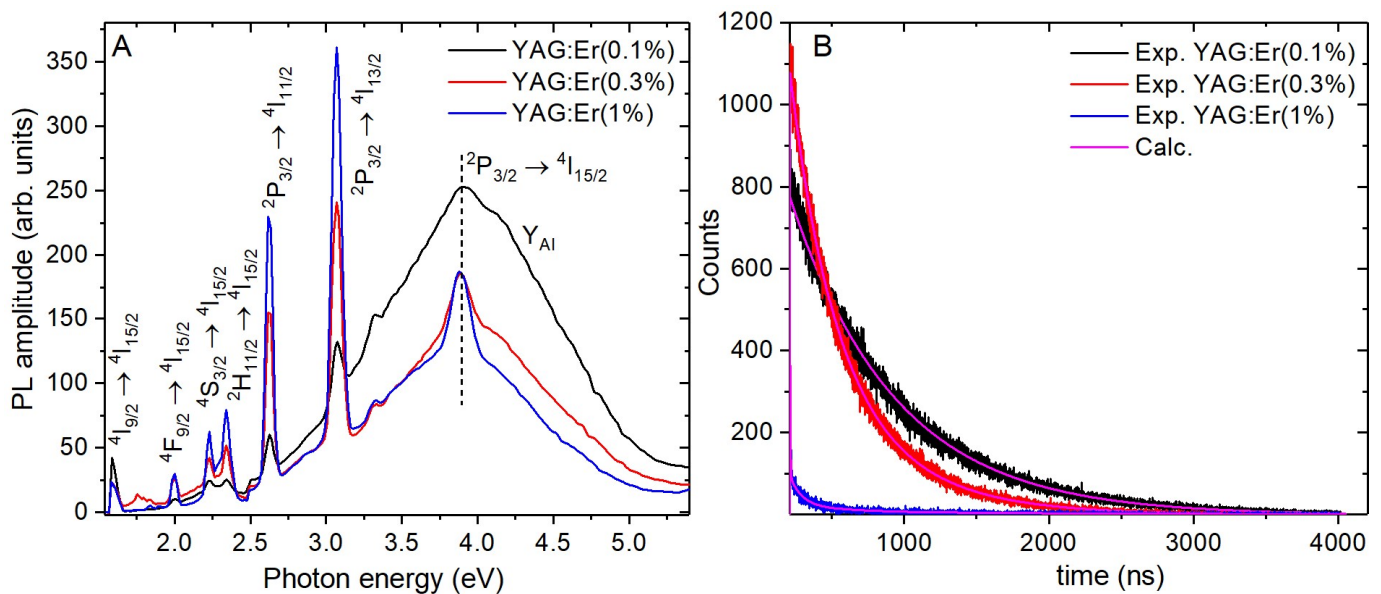


**Figure 5.** (A) RL spectra measured at 296 K under X-ray excitation in the YAG:Er (0.1%, 0.3% and 1%) samples. Specific Er<sup>3+</sup> transitions are indicated. (B) Decay curves measured at 296 K in the YAG:Er (0.1%, 0.3% and 1%) samples.

The spectral positions of narrow peaks correspond to the following Er<sup>3+</sup> 4f–4f transitions observed in RL spectra of YAG:Er [38–41]:  $4I_{9/2} \rightarrow 4I_{15/2}$  (1.59 eV),  $4F_{9/2} \rightarrow 4I_{15/2}$  (2.00 eV),  $4S_{3/2} \rightarrow 4I_{15/2}$  (2.23 eV),  $2H_{11/2} \rightarrow 4I_{15/2}$  (2.34 eV),  $2P_{3/2} \rightarrow 4I_{11/2}$  (2.61 eV),  $2P_{3/2} \rightarrow 4I_{13/2}$  (3.1 eV) and  $2P_{3/2} \rightarrow 4I_{15/2}$  (3.95 eV). Moreover, the intensity of the narrow peaks increased with the erbium content. The Stark transitions were not observed due to low spectral resolution (see Experimental).

The 3.95 eV band was attributed to  $Y_{Al}$  antisite defects [44,45]. Its intensity dropped about twice in the YAG:Er (0.3%) as compared to the YAG:Er (0.1%). It is about the same in the YAG:Er (0.3%) and YAG:Er (1%). Er substituting for Y should increase the probability for the Y substitution for Al, and therefore the  $Y_{Al}$  band should increase upon Er content. Since this was not observed (Figure 5A) the  $Y_{Al}$  energy is expected to be partly reabsorbed and then re-emitted by erbium. Erbium substitution for the Al site ( $Er_{Al}$ ) can be excluded since no other signals than  $Er_{GS}^{3+}$  and  $Er_{ES}^{3+}$ , which might be related to  $Er^{3+}$ , were detected in EPR spectra (Figure 3) at all.

To study the influence of increased erbium content on the kinetics of luminescence processes, the decay kinetics under pulsing X-ray excitation was measured in all the samples as well. The decay curves are shown in Figure 5B. They were fitted with exponentials: single-component in the YAG:Er (0.1%), two-component in the YAG:Er (0.3%) and four-component in YAG:Er (1%).

$$I = \sum_{i=1}^4 A_i \exp(-t/\tau_i) + I_0, \quad (5)$$

where  $A_i$ ,  $\tau_i$  and  $I_0$  are the amplitude and decay time constant of the  $i$ -th component and background, respectively. The background provides no valuable information, and

therefore it will not further be considered. The decay time constants and amplitudes are listed in Table 4.

**Table 4.** Decay time constants (ns) and amplitudes (arb. units).

Sample	$\tau_1$	$\tau_2$	$\tau_3$	$\tau_4$	$A_1$	$A_2$	$A_3$	$A_4$
YAG:Er (0.1%)	722.5	-	-	-	774	-	-	-
YAG:Er (0.3%)	299.3	622.2	-	-	710	369	-	-
YAG:Er (1%)	2.7	78.9	374.9	2524	309	68	19	8

Interestingly, the decay time constants, in general, shorten upon Er doping. This is also in good agreement with the drop of the  $Y_{Al}$  band (Figure 5A). Considering only the dominating amplitude ( $A_1$ ), one can see that the shortening of the corresponding decay time constant is drastic: from 722.5 ns in the YAG:Er (0.1%) through 299.3 ns in the YAG:Er (0.3%) to 2.7 ns in the YAG:Er (1%). The decay time constant of the second component ( $A_2$ ) dropped about eight times from 622.2 ns in the YAG:Er (0.3%) to 78.9 ns in the YAG:Er (1%).

This and the multicomponent origin of the decay curves can be explained in the following way. At low Er content (0.1%),  $Y_{Al}$  and Er are separated, and the single exponential with the 722.5 ns characteristic decay time belongs to the  $Y_{Al}$  band. At higher Er concentrations (0.3% and 1%), the exchange interaction between Er ions occurs as confirmed by EPR above. This leads to the advanced charge and energy transfer among erbium ions. The more Er present in the host, the higher the probability of Er appearing next to  $Y_{Al}$ . Altogether this creates conditions for advanced electrons transfer through a erbium bridge to  $Y_{Al}$ .

The faster electrons appear at  $Y_{Al}$ , the faster they can recombine with the holes. The supplement of holes is confirmed by EPR above (signals S2 and S3 in Figure 2A, see also Table 2 and the discussion below it) through  $O^-$  defects, the hole trapping centers. This also leads to the creation of several paths for charge and energy transfer resulting in the multicomponent decay curve origin. Moreover, this causes the shortening of the decay time of the  $Y_{Al}$  band (Figure 5B). This is a very important observation since it opens the way for further investigation of Er content influence on the  $Y_{Al}$  band, likely, making its luminescence even faster than observed 2.7 ns.

The rest of the long components have very low amplitudes ( $A_3 = 19$  and  $A_4 = 8$ ; this is about 15 and 40 times weaker than  $A_1 = 309$ , respectively) in the YAG:Er (1%). Therefore, they are rather the background of processes, likely due to  $Er^{3+}$  transitions that were out of the range of the X-ray equipment used for the ultrafast kinetics measurements (see Experimental).

The  $Y_{Al}$  band at 3.95 eV (Figure 5A) was not recorded in the PL spectra (Figure 4A) due to low excitation energy, 3.65 eV. The  $F^+$ -center-related band observed in PL spectra (Figure 4A) was not directly observed in the RL spectra (Figure 5A), as its intensity was low, and strong overlap with the  $Y_{Al}$  band occurs.

#### 4. Conclusions

Erbium incorporation as well as its influence on the luminescence properties of YAG single crystals grown using the micro-pulling-down technique was systematically studied. Three ion concentrations were chosen: 0.1, 0.3 and 1 at%. In particular, by using electron paramagnetic resonance (EPR), Er incorporation as a regular ion into the YAG host at the yttrium site was confirmed.

Moreover, higher concentrations (0.3 and 1 at%) led to the dipolar broadening of the  $Er^{3+}$  EPR line due to the Er–Er interaction, and Er–Er dimers were created.  $Er^{3+}$  EPR spectra were measured in the ground and first excited states for all the concentrations mentioned. The  $g$  tensors and  $^{167}Er$  hyperfine interaction (determined precisely) changed upon Er content for the ground state, whereas in the first excited state, only the hyperfine interaction changed. This was explained by the large difference in the ligand atomic orbitals and erbium first excited state to create a molecular orbital and have influence on the  $g$  tensor.

There was another signal in the EPR spectra measured at the  $g$  factor of about 2 attributed to some defect state, likely oxygen anions forming  $O_2^-$  and  $O^-$  electron and hole trapping centers. The  $O_2^-$  was observed in the YAG:Er (0.1%) whereas the  $O^-$  was detected in the YAG:Er (0.3% and 1%). The presence of the latter indicates the participation of holes in the luminescence processes. PL spectra were complex, consisting of strongly overlapped typical  $Er^{3+}$  transitions and the broad band at 3 eV attributed to the  $F^+$  center (visible only for the 0.1% Er content).

For higher Er concentrations, the  $F^+$  band was not observed, likely due to the low intensity and strong overlap with other Er-related bands or charge or energy transfer to  $Er^{3+}$ . The broadening of the Er transitions was explained by the exchange interactions existing between Er ions revealed by EPR. Radioluminescence (RL) spectra were composed of the  $Er^{3+}$  transitions as well and the other band with the maximum at about 4 eV was attributed to  $Y_{Al}$ .

The X-ray excited decay kinetics exhibited decrease of the decay time of the  $Y_{Al}$  band from hundreds of nanoseconds to nanoseconds based on the Er doping level. This was explained by the advanced electrons transfer from  $Er^{3+}$  to  $Y_{Al}$  with subsequent recombination with holes from  $O^-$ -like centers detected by EPR. The faster the electron appeared at  $Y_{Al}$ , the faster it recombined with the hole. This also paves the way for further investigation of Er content influence on fast and, likely, ultrafast processes of  $Y_{Al}$  luminescence.

**Author Contributions:** Conceptualization, M.B.; Methodology, J.P. and F.L.; Validation, J.P. and S.C.; Formal analysis, M.B., A.M.G.-B., Z.R., K.R., V.B. and S.C.; Investigation, M.B., A.M.G.-B., Z.R., K.R., V.B. and S.C.; Resources, J.P. and F.L.; Data curation, M.B.; Writing—original draft, M.B. and A.M.G.-B.; Writing—review & editing, J.P., F.L., Z.R., K.R. and V.B.; Visualization, A.M.G.-B., F.L., Z.R., K.R., V.B. and S.C.; Supervision, M.B. All authors have read and agreed to the published version of the manuscript.

**Funding:** This research received no external funding.

**Institutional Review Board Statement:** Not applicable.

**Informed Consent Statement:** Not applicable.

**Data Availability Statement:** Not applicable.

**Conflicts of Interest:** The authors declare no conflict of interest.

## References

1. Zorenko, Y.; Gorbenko, V.; Zorenko, T.; Savchyn, V.; Batentschuk, M.; Osvet, A.; Brabec, C. Luminescent properties and energy transfer processes in YAG:Er single crystalline films. *J. Lumin.* **2014**, *154*, 198–203. [[CrossRef](#)]
2. Dobretsova, E.A.; Kuznetsov, S.V.; Chikulina, I.S.; Nikova, M.S.; Tarala, V.A.; Vakalov, D.S.; Zhmykhov, V.; Tsvetkov, V.B. Optical properties of 50 at.%  $Er^{3+}$ :YAG ceramics. In Proceedings of the 2020 International Conference Laser Optics (ICLO), St. Petersburg, Russia, 2–6 November 2020; p. 1. [[CrossRef](#)]
3. Liu, J.; Liu, Q.; Li, J.; Ivanov, M.; Ba, X.; Yuan, Y.; Lin, L.; Chen, M.; Liu, W.; Kou, H.; et al. Influence of doping concentration on microstructure evolution and sintering kinetics of Er:YAG transparent ceramics. *Opt. Mater.* **2014**, *37*, 706–713. [[CrossRef](#)]
4. Chen, Z.; Trofimov, A.A.; Jacobsohn, L.G.; Xiao, H.; Kornev, K.G.; Xu, D.; Peng, F. Permeation and optical properties of YAG:Er<sup>3+</sup> fiber membrane scintillators prepared by novel sol-gel/electrospinning method. *J. Sol-Gel Sci. Technol.* **2017**, *83*, 35–43. [[CrossRef](#)]
5. Nobari, N.N.; Tabavar, A.; Sadeghi, S.; Dehghani, A.; Kalantari, Y.; Ghassemi, M.; Atefi, N.; Goodarzi, A. A systematic review of the comparison between needling (RF-needling, meso-needling, and micro-needling) and ablative fractional lasers (CO<sub>2</sub>, erbium YAG) in the treatment of atrophic and hypertrophic scars. *Lasers Med. Sci.* **2023**, *38*, 67. [[CrossRef](#)] [[PubMed](#)]
6. Darafsheh, A.; Hutchens, T.C.; Fardad, A.; Antoszyk, A.N.; Ying, H.S.; Fried, N.M.; Astratov, V.N. *Contact Focusing Multimodal Probes for Potential Use in Ophthalmic Surgery with the Erbium:YAG Laser*; Manns, F., Söderberg, P.G., Ho, A., Eds.; SPIE BiOS: San Francisco, CA, USA, 2013; p. 856729. [[CrossRef](#)]
7. Feng, C.; Ding, Y.; Tang, L.; Gui, Y.; Shen, X.; He, L.; Lu, X.; Leung, W.K. Adjunctive Er:YAG laser in non-surgical periodontal therapy of patients with inadequately controlled type 2 diabetes mellitus: A split-mouth randomized controlled study. *J. Periodontol Res.* **2022**, *57*, 63–74. [[CrossRef](#)] [[PubMed](#)]
8. Pushkin, A.V.; Potemkin, F.V. Features of the High-Power (up to 1 MW, 100 mJ) 3- $\mu$ m Nanosecond Laser Pulse Generation in Erbium-Doped Crystals in the Repetitively Pulsed Regime. *JETP Lett.* **2022**, *116*, 514–521. [[CrossRef](#)]

9. Chen, X.; Wu, Y.; Wei, N.; Qi, J.; Li, Y.; Zhang, Q.; Hua, T.; Zhang, W.; Lu, Z.; Ma, B.; et al. Fabrication and spectroscopic properties of Yb/Er:YAG and Yb, Er:YAG transparent ceramics by co-precipitation synthesis route. *J. Lumin.* **2017**, *188*, 533–540. [[CrossRef](#)]
10. He, M.; Bao, N.; Qi, R.; Wu, Y.; Liu, M. A randomized, prospective pilot study for comparison of a triple combination of 2940 nm Er: YAG Laser and triamcinolone acetonide solution with either 308 nm excimer laser or 0.1% tacrolimus in treatment of stable segmental vitiligo. *Dermatol. Ther.* **2022**, *35*. [[CrossRef](#)] [[PubMed](#)]
11. Zhmykhov, V.; Dobretsova, E.; Tsvetkov, V.S.; Nikova, M.; Chikulina, I.; Vakalov, D.; Tarala, V.; Pyrkov, Y.; Kuznetsov, S.; Tsvetkov, V. Judd–Ofelt Analysis of High Erbium Content Yttrium–Aluminum and Yttrium–Scandium–Aluminum Garnet Ceramics. *Inorganics* **2022**, *10*, 170. [[CrossRef](#)]
12. Celiksoz, O.; Yilmaz, N.; Balin, E. Effect of Er: YAG laser on repair bond strength of a nano-hybrid composite. *J. Stomatol.* **2022**, *75*, 122–129. [[CrossRef](#)]
13. Walsh, J.T., Jr.; Deutsch, T.F. Er:YAG laser ablation of tissue: Measurement of ablation rates. *Lasers Surg. Med.* **1989**, *9*, 327–337. [[CrossRef](#)] [[PubMed](#)]
14. Yan, K.; Song, J.; Liu, X.; Zhang, Y.; Qiu, Y.; Jiao, J.; Wu, M. Effect of Er:YAG laser pretreatment on glass–ceramic surface in vitro. *Lasers Med. Sci.* **2022**, *37*, 3177–3182. [[CrossRef](#)] [[PubMed](#)]
15. Yang, S.; Yun, Z.; Zhao, L.; Cheng, M.; Zhou, T.; Huang, E.; Guo, Y.; Xu, Y.; Yin, W.; Chen, X.; et al. Temperature Changes in Oral All-Ceramic Materials with Different Optical Properties under Er:YAG Laser Irradiation. *Dis. Markers* **2022**, *2022*, 3443891. [[CrossRef](#)] [[PubMed](#)]
16. Galeotti, A.; D’Antò, V.; Gentile, T.; Galanakis, A.; Giancristoforo, S.; Uomo, R.; Romeo, U. Er:YAG Laser Dental Treatment of Patients Affected by Epidermolysis Bullosa. *Case Rep. Dent.* **2014**, *2014*, 421783. [[CrossRef](#)] [[PubMed](#)]
17. Cao, W.; Becerro, A.I.; Castaing, V.; Fang, X.; Florian, P.; Fayon, F.; Zanghi, D.; Veron, E.; Zandonà, A.; Genevois, C.; et al. Highly Nonstoichiometric YAG Ceramics with Modified Luminescence Properties. *Adv. Funct. Mater.* **2023**, 202213418. [[CrossRef](#)]
18. Pugina, R.S.; da Silva, D.L.; Riul, A.; da Silva-Neto, M.L.; Gomes, A.S.; Caiut, J.M.A. Silk fibroin-Yb<sup>3+</sup>/Er<sup>3+</sup>:YAG composite films and their thermometric applications based on up-conversion luminescence. *Polymer* **2022**, *241*, 124541. [[CrossRef](#)]
19. Pokorný, M.; Páterek, J.; Nikl, M.; Sýkorová, S.; Stehlík, A.; Polák, J.; Houžvička, J. Concentration dependence of energy transfer Ce<sup>3+</sup>→Er<sup>3+</sup> in YAG host. *Opt. Mater.* **2018**, *86*, 338–342. [[CrossRef](#)]
20. Asatryan, H.; Shakurov, G.; Petrosyan, A.; Hovannesyanyan, K. Wideband EPR-spectroscopy of Y<sub>3</sub>Al<sub>5</sub>O<sub>12</sub>:Er<sup>3+</sup>, (Y<sub>0.9</sub>Lu<sub>0.1</sub>)<sub>3</sub>Al<sub>5</sub>O<sub>12</sub>:Er<sup>3+</sup> and Y<sub>3</sub>Al<sub>5</sub>O<sub>12</sub>:Fe<sup>2+</sup> crystals. *Magn. Reson. Solids* **2019**, *21*. [[CrossRef](#)]
21. Yoshikawa, A.; Nikl, M.; Boulon, G.; Fukuda, T. Challenge and study for developing of novel single crystalline optical materials using micro-pulling-down method. *Opt. Mater.* **2007**, *30*, 6–10. [[CrossRef](#)]
22. Yoshikawa, A.; Chani, V. Growth of Optical Crystals by the Micro-Pulling-Down Method. *MRS Bull.* **2009**, *34*, 266–270. [[CrossRef](#)]
23. Rajiv, P.; Dinnebier, R.E.; Jansen, M. “Powder 3D Parametric”—A program for Automated Sequential and Parametric Rietveld Refinement Using Topas. *Mater. Sci. Forum* **2010**, *651*, 97–104.
24. Chang, Y.-Y.; Remes, Z.; Micova, J. MASS PRODUCTION OF HYDROGENATED ZnO NANORODS. In Proceedings of the 11th International Conference on Nanomaterials-Research & Application, Hotel Voronez I, Brno, Czech Republic, 16–18 October 2019.
25. Chang, Y.-Y.; Stuchlík, J.; Neykova, N.; Souček, J.; Remeš, Z. Optical properties of the plasma hydrogenated ZnO thin films. *J. Electr. Eng.* **2017**, *68*, 70–73. [[CrossRef](#)]
26. Mooney, J.; Kambhampati, P. Get the Basics Right: Jacobian Conversion of Wavelength and Energy Scales for Quantitative Analysis of Emission Spectra. *J. Phys. Chem. Lett.* **2013**, *4*, 3316–3318. [[CrossRef](#)]
27. Stoll, S.; Schweiger, A. EasySpin, a comprehensive software package for spectral simulation and analysis in EPR. *J. Magn. Reson.* **2006**, *178*, 42–55. [[CrossRef](#)]
28. Callens, R.; Callens, F.; Matthys, P.; Boesman, E. EPR of a New 0; Centre in HCl. *Phys. Stat. Sol. (b)* **1988**, *148*, 683–688. [[CrossRef](#)]
29. Baker, J.; Robinson, P. EPR of a new defect in natural quartz: Possibly O-2. *Solid State Commun.* **1983**, *48*, 551–554. [[CrossRef](#)]
30. Hagston, W. Implications of the theory for defect centres having g factors close to the free spin values. *J. Phys. C: Solid State Phys.* **1970**, *3*, 1233–1241. [[CrossRef](#)]
31. Singh, V.; Rai, V.K.; Watanabe, S.; Rao, T.K.G.; Ledoux-Rak, I.; Kwak, H.-Y. Infrared emissions, visible up-conversion, thermoluminescence and defect centres in Er<sub>3</sub>Al<sub>5</sub>O<sub>12</sub> phosphor obtained by solution combustion reaction. *Appl. Phys. B Laser Opt.* **2010**, *101*, 631–638. [[CrossRef](#)]
32. Etschmann, B.; Streltsov, V.; Ishizawa, N.; Maslen, E.N. Synchrotron X-ray study of Er<sub>3</sub>Al<sub>5</sub>O<sub>12</sub> and Yb<sub>3</sub>Al<sub>5</sub>O<sub>12</sub> garnets. *Acta Crystallogr. Sect. B Struct. Sci.* **2001**, *57*, 136–141. [[CrossRef](#)]
33. Buryi, M.; Remeš, Z.; Babin, V.; Artemenko, A.; Vaněček, V.; Dragounová, K.A.; Landová, L.; Kučerková, R.; Mičová, J. Transformation of free-standing ZnO nanorods upon Er doping. *Appl. Surf. Sci.* **2021**, *562*. [[CrossRef](#)]
34. Buryi, M.; Laguta, V.; Babin, V.; Laguta, O.; Brik, M.; Nikl, M. Rare-earth ions incorporation into Lu<sub>2</sub>Si<sub>2</sub>O<sub>7</sub> scintillator crystals: Electron paramagnetic resonance and luminescence study. *Opt. Mater.* **2020**, *106*, 109930. [[CrossRef](#)]
35. Abragam, A.; Bleaney, B. *Electron Paramagnetic Resonance of Transition Ions*; Oxford University Press: Oxford, UK, 2012.
36. Nakatsuka, A.; Yoshiasa, A.; Yamanaka, T. Cation distribution and crystal chemistry of Y<sub>3</sub>Al<sub>5-x</sub>Ga<sub>x</sub>O<sub>12</sub> (0 ≤ x ≤ 5) garnet solid solutions. *Acta Crystallogr. Sect. B Struct. Sci.* **1999**, *55*, 266–272. [[CrossRef](#)] [[PubMed](#)]
37. Buryi, M.; Havlák, L.; Jarý, V.; Bárta, J.; Laguta, V.; Beitlerová, A.; Li, J.; Chen, X.; Yuan, Y.; Liu, Q.; et al. Specific absorption in Y<sub>3</sub>Al<sub>5</sub>O<sub>12</sub>:Eu ceramics and the role of stable Eu<sup>2+</sup> in energy transfer processes. *J. Mater. Chem. C* **2020**, *8*, 8823–8839. [[CrossRef](#)]

38. Burdick, G.W.; Gruber, J.B.; Nash, K.L.; Chandra, S.; Sardar, D.K. Intensity parametrizations for electric-dipole transitions between Stark components in  $\text{Er}^{3+}:\text{Y}_3\text{Al}_5\text{O}_{12}$ . *J. Alloys Compd.* **2009**, *488*, 632–637. [[CrossRef](#)]
39. Gruber, J.B.; Hills, M.E.; Seltzer, M.D.; Turner, G.A.; Morrison, C.A.; Kokta, M.R. Spectroscopic analysis of  $\text{Er}^{3+}(4f_{11})$  in  $\text{Y}_3\text{Sc}_2\text{Al}_3\text{O}_{12}$ . *Chem. Phys.* **1990**, *144*, 327–342. [[CrossRef](#)]
40. Spangler, L.H.; Farris, B.; Filer, E.D.; Barnes, N.P. A computational study of host effects on  $\text{Er}^{3+}$  upconversion and self-quenching efficiency in ten garnets. *J. Appl. Phys.* **1996**, *79*, 573. [[CrossRef](#)]
41. Skaudzius, R.; Juestel, T.; Kareiva, A. Luminescence properties of  $\text{Ln}^{3+}$ -doped ( $\text{Ce}^{3+}$ ,  $\text{Eu}^{3+}$ ,  $\text{Tb}^{3+}$  or  $\text{Er}^{3+}$ ) Mixed-Metals  $\text{Y}_3(\text{Al}, \text{In})_5\text{O}_{12}$  and  $\text{Y}_3\text{Al}_{4.75}\text{Cr}_{0.25}\text{O}_{12}$  garnets synthesized by Sol–Gel method. *Mater. Chem. Phys.* **2016**, *170*, 229–238. [[CrossRef](#)]
42. Pujats, A.; Springis, M. The F-type centres in YAG crystals. *Radiat. Eff. Defects Solids* **2001**, *155*, 65–69. [[CrossRef](#)]
43. Zych, E.; Brecher, C. Temperature dependence of host-associated luminescence from YAG transparent ceramic material. *J. Lumin.* **2000**, *90*, 89–99. [[CrossRef](#)]
44. Babin, V.; Blazek, K.; Krasnikov, A.; Nejezchleb, K.; Nikl, M.; Savikhina, T.; Zazubovich, S. Luminescence of undoped LuAG and YAG crystals. *Phys. Status Solidi (C)* **2005**, *2*, 97–100. [[CrossRef](#)]
45. Haven, D.T.; Dickens, P.T.; Weber, M.H.; Lynn, K.G. Yttrium antisite reduction and improved photodiode performance in Ce doped  $\text{Y}_3\text{Al}_5\text{O}_{12}$  by Czochralski growth in alumina rich melts. *J. Appl. Phys.* **2013**, *114*, 043102. [[CrossRef](#)]

**Disclaimer/Publisher’s Note:** The statements, opinions and data contained in all publications are solely those of the individual author(s) and contributor(s) and not of MDPI and/or the editor(s). MDPI and/or the editor(s) disclaim responsibility for any injury to people or property resulting from any ideas, methods, instructions or products referred to in the content.